

THE HYDROGEN EPOCH OF REIONIZATION ARRAY DISH: CHARACTERIZATION WITH ELECTROMAGNETIC SIMULATIONS

EWALL-WICE AARON^{1,2}, ABRAHAM NEBEN^{1,2}, NIPANJANA PATRA⁵, THYAGARAJAN NITHYANANDAN⁶, RICHARD BRADLEY^{3,4},
 JACQUELINE HEWITT^{1,2}, ALI S. ZAKI⁵, BOWMAN JUDD⁶, CHENG CARINA⁵, DEBOER DAVID⁵, PARSONS AARON⁵, VENTER
 MARIET⁷ AND OTHERS.

Draft version November 5, 2015

ABSTRACT

Using electromagnetic simulations, we assess the spectral properties of the antenna element of the Hydrogen Epoch of Reionization Array (HERA) in order to both establish a specification for the degree of spectral structure that is permissible to sufficiently isolate foregrounds and allow a detection of the cosmological 21 cm signal and verify direct laboratory measurements of the dish characteristics. We find that our simulations are in good agreement with field measurements. Using simulations of foregrounds, we find that the ≈ -40 dB response at 60 ns of the HERA dish is sufficient to isolate the cosmological 21 cm signal ≈ 0.2 hMpc⁻¹ at $z \approx 8.5$ and obtain a high signal to noise detection of the power spectrum.

1. INTRODUCTION

Observations of the redshift 21 cm radiation neutral hydrogen in the intergalactic medium (IGM) have the potential to illuminate the hitherto unobserved *dark ages* and *cosmic dawn*, revolutionizing our understanding of the first UV and X-ray sources in the universe and how their properties influenced galactic evolution (see Furlanetto et al. (2006), Morales & Wyithe (2010), and Pritchard & Loeb (2012) for reviews). As of now, two major experimental endeavors are underway to make a first detection of the 21 cm signal with most focusing on the Epoch of Reionization (EoR) in which UV photons from early galaxies transformed the hydrogen in the universe from neutral to ionized. The first involves measuring the sky-averaged global signal and is being pursued by experiments such as EDGES (Bowman & Rogers 2010), LEDA (Greenhill & Bernardi 2012), DARE (Burns et al. 2012), SciHi (Voytek et al. 2014), and BIGHORNS (Sokolowski et al. 2015) coming online in their planning stages or taking data. The second attempts to observe spatial fluctuations in the 21 cm emission using radio interferometers. As of now, a first generation of interferometry experiments are taking data in an attempt to make a first statistical detection of the power spectrum of 21 cm brightness temperature fluctuations. These include the Giant Metrewave Telescope (GMRT) (Paciga et al. 2013), the Low Frequency Array (LOFAR), (van Haarlem et al. 2013), the Murchison Widefield Array (?) and the Precision Array for Probing the Epoch of Reionization (PAPER) (Parsons et al. 2010).

The primary obstacle to obtaining a high redshift detection of the cosmological signal through both of these methods is the existence of foregrounds that are $\sim 10^5 - 10^6$ times brighter. While requiring much greater

sensitivity to global-signal experiments, interferometers have the advantage that these spectrally smooth foregrounds naturally avoid a significant region of k -space, known as the *EoR window*, occupying a region known as the *wedge* (Datta et al. 2010; Vedantham et al. 2012; Parsons et al. 2012; Thyagarajan et al. 2013; Liu et al. 2014a,b), however any structure in the frequency response of the instrument has the potential to leak foregrounds into the EoR window, masking our signal. Indeed, low level spectral structures in the analogue and digital signal chains on the initial buildout of the MWA are proving to be a significant obstacle (Dillon et al. 2015; Ewall-Wice et al. submitted 2015; Beardsley et al. in preparation).

While, in principle, spectral structure in the band-pass of the instrument may be removed in calibration, simulations show that any mismodeling of emission and the primary beam, potentially below the confusion limit, will mix the significant spectral structure on long baselines into short ones, masking the signal entirely (Barry et al. in preparation). While redundant calibration (Wieringa 1992; Liu & Tegmark 2011; Zheng et al. 2014) is able to calibrate the independent of a detailed model of the sky, any direction-dependent chromatic structure in the primary beam of the instrument introduces additional degrees of freedom that must be modeled, potentially leading to signal loss and the introduction of spurious spectral structure due to unmodeled foregrounds in long baselines. Because of our limited knowledge of foregrounds at low-frequency and the fidelity of calibration algorithms, the only sure way of building an instrument that will guarantee a detection of the redshifted 21 cm emission is to design it such that all spectral structure in the signal chain is limited to a finite region of delay space, well below the wedge.

The Hydrogen Epoch of Reionization Array (HERA) is an instrument currently taking first observations in the Karoo in South Africa with the ultimate goal of detecting the power spectrum of 21 cm brightness temperature fluctuations at high signal-to-noise (SNR) (Pober et al. 2014). A central principle in HERA's design is that it be calibration fail-safe such that a detection of

¹ MIT Kavli Institute for Cosmological Physics

² MIT Dept. of Physics

³ National Radio Astronomy Obs., Charlottesville VA

⁴ Dept. of Astronomy, U. Virginia, Charlottesville VA

⁵ Astronomy Dept. U. California, Berkeley CA

⁶ School of Earth and Space Exploration, Arizona State U., Tempe AZ

FIG. 1.— The HERA primary antenna element-one of 19 undergoing currently taking the first observations in the Karoo in South Africa. The antenna consists of a sleeved dipole suspended within a 2 m diameter skirt, five meters above the ground at the focal point of a 14 m diameter dish.

the signal is guaranteed, even if the chromaticity of the instrument is not calibrated out. This paper and its companions (Neben et al. submitted; Patra et al. submitted; Thyagarajan et al. submitted) describe a multifaceted approach to establishing a stringent specification on the spectral structure permissible for HERA to be calibration fail-safe and determine to what extent its design meets these requirements. We accomplish this by establishing a spec with simulations of foregrounds (?) and verifying that HERA primary antenna element meets this spec with reflectometry (Patra et al. submitted) and Or-bcomm beam mapping (Neben et al. submitted). These measurements are verified with detailed electromagnetic simulations which we describe in this work.

This paper is organized as follows. In § 2 we lay out our analytic framework for describing the impact of reflections and spectral structure on foreground leakage in delay-transform power spectra. In § 3 we describe our electromagnetic simulations of the HERA dish element. In § 4 we compare our simulation results to direct measurements of the primary dish element and in § 5 we apply our electromagnetic simulation results to simulations of foregrounds to determine the extent that the HERA dish's chromatic structure pollutes the EoR window and their impact on HERA's overall sensitivity. We conclude in § 6.

2. THE IMPACT OF REFLECTIONS ON DELAY-TRANSFORM POWER SPECTRA

In this section, we show how reflections in the analogue signal path of an antenna lead to foreground contamination of the EoR window. HERA's primary antenna element consists of a sleeved dipole element suspended 5 m above the focus of a 14 m diameter parabolic dish (Fig. 1).

We show in Appendix A that if an astronomical radio signal with time dependence at the location of the feed, $s(\hat{\mathbf{k}}, t)$, experience reflections within the dish such that the voltage recorded in the feed is

$$v_i(t) = \sum_n r_i(\hat{\mathbf{k}}, \tau_n) s(\hat{\mathbf{k}}, t - \tau_n) \quad (1)$$

Then the resulting visibilities obtained by cross correlating antenna i and antenna j are given by

$$V'_{ij}(f) = \sum_{m,n} \int d\Omega R_{ij}(\hat{\mathbf{k}}, \Delta\tau_{mn}) e^{2\pi i \Delta\tau_{mn} f} e^{2\pi i \mathbf{u}_{ij} \cdot \hat{\mathbf{k}}} I(f, \hat{\mathbf{s}}), \quad (2)$$

where $R_{ij}(\hat{\mathbf{s}}, \Delta\tau_{mn}) = r_m r_n^*$, $I(f, \hat{\mathbf{s}})$ is the intensity of the signal on the sky, and can be decomposed into foregrounds and signal

$$I(f, \hat{\mathbf{s}}) = I_{fg}(f, \hat{\mathbf{s}}) + I_{21}(f, \hat{\mathbf{s}}) \quad (3)$$

While I_{fg} is on the order of 10^6 times larger than I_{21} , the continuum emission from foregrounds is expected to be spectrally smooth. Hence, a *delay transform* defined by

$$\tilde{V}_{ij}(\tau) = \int df e^{-2\pi i \tau f} V_{ij}(f) \quad (4)$$

should, in principle, separate the foregrounds from the signal with foregrounds occupying the wedge. However, the introduction of the chromatic $e^{2\pi i \Delta\tau_{mn}}$ terms leads to foreground contamination being convolved out to higher delays.

$$\tilde{V}'_{ij}(\tau) = \sum_{m,n} \tilde{V}_{ij,FG}^{mn}(\tau - \Delta\tau_{mn}) + \tilde{V}_{ij,21}^{mn}(\tau - \Delta\tau_{mn}) \quad (5)$$

where V_{ij}^{mn} is a visibility resulting from the effective primary beam, $R_{ij}(\hat{\mathbf{k}}, \Delta\tau_{mn})$, at delay $\Delta\tau_{mn}$ induced by the reflections.

$$V_{ij}^{mn} = \int d\Omega R_{ij}(\hat{\mathbf{s}}, \Delta\tau_{mn}) I(f, \hat{\mathbf{s}}) e^{2\pi i \mathbf{u}_{ij} \cdot \hat{\mathbf{s}}} \quad (6)$$

The delay transform power spectrum estimate, \hat{P} , is proportional to $|\tilde{V}'_{ij}|^2$, hence

$$\begin{aligned} \hat{P} &\propto |\tilde{V}_{ij,FG}(\tau)|^2 + |\tilde{V}_{ij,21}(\tau)|^2 + 2\text{Re}(\tilde{V}_{ij,21}(\tau) \tilde{V}_{ij,FG}^*(\tau)) \\ &+ \sum_{|\Delta\tau_{mn}| > 0} 2\text{Re} \left[\tilde{V}_{ij}^*(\tau) \tilde{V}_{ij}^{mn}(\tau - \Delta\tau_{mn}) \right] \\ &+ \sum_{\substack{|\Delta\tau_{op}| > 0 \\ |\Delta\tau_{mn}| > 0}} \tilde{V}_{ij}^{mn}(\tau - \Delta\tau_{mn}) \tilde{V}_{ij}^{op*}(\tau - \Delta\tau_{op}) \end{aligned} \quad (7)$$

In the absence of reflections, only the top line of equation 7 would enter the delay power spectrum estimate. The following lines involve the translation of the signal (including foregrounds and signal) out to the delay of each reflection and weighted by the effective primary beam of the reflection. Since each translated visibility is intrinsically $\sim 10^6$ times brighter than the signal, any reflection with a delay large enough to place it within the EoR window, must be sufficiently attenuated by $R_{ij}(\hat{\mathbf{k}}, \Delta\tau_{mn})$.

To get a better idea for what spec this sets on the voltage response of our dish we examine, in more detail, the case where r_0 at $(\tau = 0)$ is significantly greater than the other coefficients as we might expect for a dish with a relatively smooth gain. Then we can approximate equation 7 to linear order in r_i ,

$$\tilde{V}'_{ij}(\tau) \approx \tilde{V}_{ij} + \sum_{m>0} \tilde{V}_{ij}^{m0}(\tau - \tau_m) \quad (8)$$

If we make the assumption that the beam can be factored into a frequency dependent and frequency dependent term, $r_i(\hat{\mathbf{k}}, \tau) = a_i(\hat{\mathbf{k}}) g_i(\tau)$ then we have

$$\tilde{V}'_{ij} \approx \tilde{V}_{ij}(\tau) + \sum_{m>0} r_m \tilde{V}_{ij}(\tau - \tau_m) \quad (9)$$

Hence, for a delay response dominated by the 0-delay mode, as we might expect in an antenna element with smooth gain, the delay transformed visibilities are effectively convolved with the *voltage response*, not the square of the voltage response as we might naively expect. A more compact writing the impact of the spectral structure of a separable beam on foregrounds would be

$$\tilde{V}'_{ij}(\tau) = \left[(g_i \star g_j^*) \star \tilde{V}_{ij} \right](\tau) \quad (10)$$

3.1. The Simulations

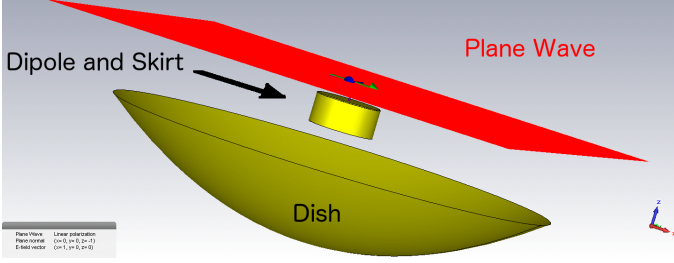


FIG. 2.— A rendering of our time domain simulation at $t = 0$, demonstrating the geometry and setup of our electromagnetic simulation. The plane wave is started just above the feed (red plane).

As a result, one should compare the amplitude of the voltage delay response of the antenna with the ratio between foregrounds and signal when

In this paper, we study $r_i(\hat{\mathbf{k}}, \Delta\tau)$ for the HERA antenna element to verify that it both meets the spec and agrees with direct measurements of the antenna element with reflectometry (Patra et al. submitted) and Orbcomm measurements (Neben et al. submitted). We also explore the implications of the performance of $r_i(\hat{\mathbf{k}}, \tau)$ on the scientific bottom line for EoR experiments, using the Fisher Matrix Formalism.

3. ELECTROMAGNETIC SIMULATIONS OF THE HERA DISH ELEMENT

In Fig. 2 we show the geometry of the electromagnetic simulation. **Rich: fill in the details here**

3.2. Deconvolving the Response Function

In our simulation, we obtain the voltage at the feed output as a function of time which we will call $v_{out}(t)$. It is related to the input plane wave through the equation

$$v_{out}(t, \theta = 0) = \sum_n r_n(\theta = 0) v_{in}(t - \tau_n, \theta = 0), \quad (11)$$

which is essentially a convolution in time of $r_n(\theta = 0)$ with the input plane wave. We may undo this convolution by taking a discrete Fourier transform of both v_{out} and v_{in} in time, dividing them in Fourier space, and taking an inverse DFT back. Our simulation output is sampled at even time intervals so we may use and FFT.

$$\hat{\mathbf{r}}(\theta = 0) = \mathcal{F}^{-1} \left[\frac{\mathcal{F} \mathbf{v}_{out}(\theta = 0)}{\mathbf{v}_{in}(\theta = 0)} \right] \quad (12)$$

where \mathcal{F} is the Fourier transform matrix for a 1d vector of length N .

$$\mathcal{F}_{mn} = e^{2\pi i m n / N} \quad (13)$$

In Fig. 4 we show the amplitude of the Fourier transform of our Gaussian input, centered at 150 MHz along with the voltage response. Since our input is band limited between ≈ 20 and 280 MHz, the direct ratio of our voltage response and input wave is dominated by numerical noise outside of this range. We eliminate these numerical artifacts by multiplying our ratio by a Hamming window between 50 MHz and 250 MHz and set our estimate to zero elsewhere. From a physical standpoint, this is sensible since 21 cm experiments only observe a limited bandwidth. PAPER's correlator, which will initially

serve as the HERA backend samples over a 100 MHz instantaneous frequency interval. Hence analogue filtering is applied to limit the incoming signal within a finite bandwidth and prevent aliasing.

4. RESULTS AND COMPARISON TO REFLECTOMETRY DATA

4.1. The Delay Response at Zenith

In Fig. 5, we show the filtered response function deconvolved from our electromagnetic simulations. The response of the dish rapidly dies off as a function of time. After ≈ 90 ns, we observe lobed structures with a period of ≈ 30 ns which corresponds to the geometrical delay between the feed and the dish apex, indicating that the large τ roll off is dominated by reflections between the feed and the dish.

Our simulations are intended to verify direct reflectometry measurements taken on a prototype of the HERA feed and dish in Green Bank, presented in (Patra et al. submitted). For the readers convenience, we briefly explain the reflectometry measurement here before comparing them to our simulation.

In the reflectometry measurement, a signal is sent from a Vector Network Analyzer (VNA) via a coaxial cable (which is calibrated out) into the back of the feed. The VNA then measures the ratio between returned and transmitted power as a function of frequency, $S_{11}(f)$. A fundamental difference between the reflectometry measurement and the delay response that we are attempting to obtain is that at zero delay, S_{11} is measuring the reflection of the input wave off of the back of the feed while in the delay response of the antenna, the zero delay reflection is the fraction of the electromagnetic wave off of the sky that is accepted by the feed. To obtain $\hat{\rho}$, we must correct for this difference. It is shown in (Patra et al. submitted) that the correction is

$$\hat{\rho}(f) = \frac{\Gamma_a(f)}{1 - \Gamma_a(f)} [S_{11}(f) - \Gamma_a(f)] + 1 - \Gamma_a(f). \quad (14)$$

Applying this transformation to $S_{11}(f)$ and taking a DFT into the time domain over a band of 100 – 200 MHz, we obtain a measurement based estimate of the dish response function at zenith which is plotted in Fig. 5 alongside our simulation result. The general trends of the two lines are in excellent agreement though the phases of the reflections at large time scales are ≈ 10 ns out of phase. As the long term delay structure of the delay response determines to what extent foregrounds leak out of the wedge, our simulations verify our measurement of the HERA dish's key performance feature.

4.2. The Delay Response of the Sidelobes

After observing decent agreement between simulations and data, we now use our time-domain simulations to probe the side-lobe structure of the dish which are currently inaccessible to our experimental setup. Understanding the delay structure of the sidelobes is critical for several reasons. First, the sidelobes represent the largest delays occupied by foregrounds, hence the closest to the EoR window which we wish to keep foreground-free. While spectral leakage of sources at zenith may place them somewhere within the wedge, any spectral structure in the sidelobes is guaranteed to place these

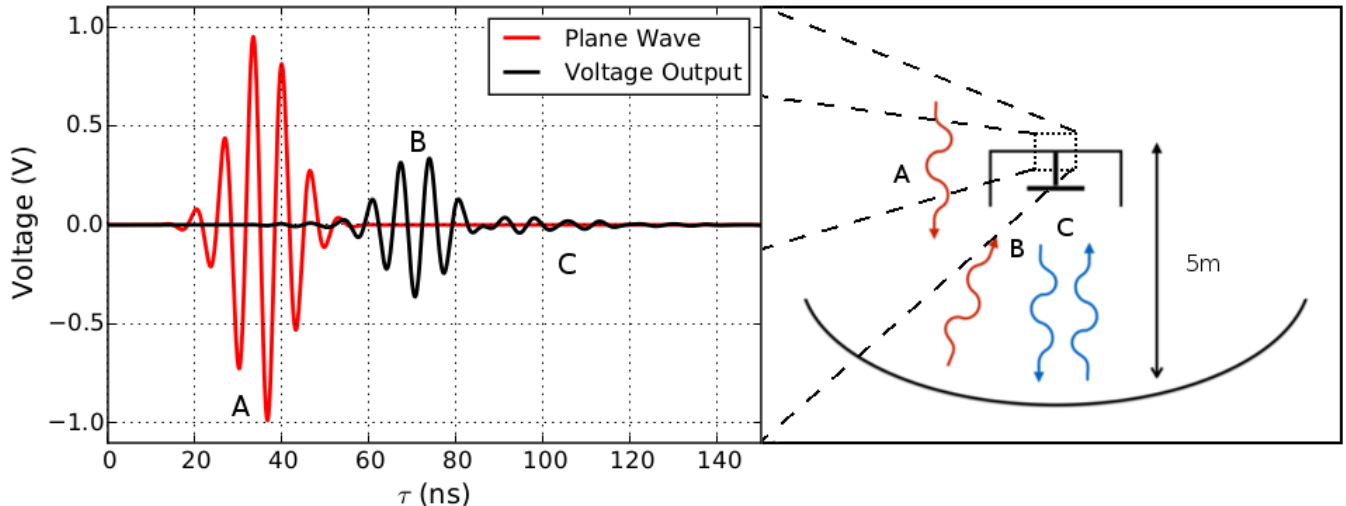


FIG. 3.— An illustration of our simulation products and their origin in the HERA antenna geometry. A plane wave is injected from above the feed (red line). The amplitude of the electric field of the plane wave at output of the feed along with the voltage at the feed terminal outputs is recorded (black line). The feed in our simulation is situated 5 m above the bottom of the dish, hence there is a ≈ 30 ns delay between when the plane wave passes the terminal for the first time (A) and when it is first absorbed in the dipole (B), leading to the voltage response. Of concern to 21 cm experiments are the subsequent reflections between the feed and the dish (C) which can lead to large delay contamination of the EoR window.

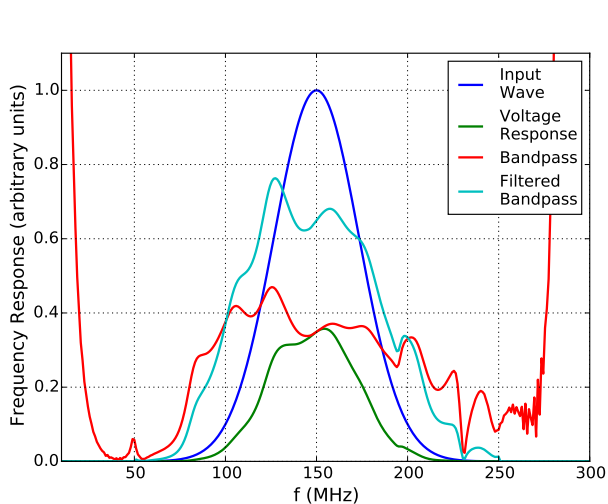


FIG. 4.— The absolute value of the discrete Fourier transform of our simulation outputs. We obtain the effective response function of the dish by Fourier transforming the voltage output from our dish (green line) and dividing by the Fourier transform of the input wave (blue line). The simple ratio is plotted as a red line. Since our input is limited to frequencies between ≈ 20 and 280 MHz, there is significant numerical noise that will effect our result outside of this region which we see in the divergence of the red line towards the edges of the plot. To eliminate this noise, we multiply by a Hamming window between 50 and 250 MHz and set our estimate to zero elsewhere. The Fourier transform of our response estimate with the filter applied is shown as a cyan line.

sources directly inside of the window. Second, the forshortening of diffuse structure near the horizon due to wide-field projection effects leads to a significant amount of foreground power entering at these delays, generally making them the most contaminated region of the wedge outside of the central lobe and leading to the so called “pitchfork” (Thyagarajan et al. 2015b,a).

We first attempt to explore the Dish sidelobe structure by running high resolution spatial beam maps **Rich fill in details of running 2D beam simulations.** How-

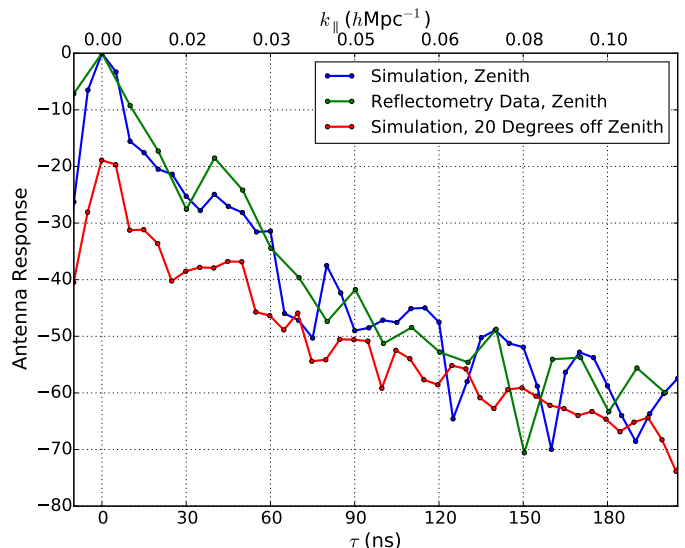


FIG. 5.— The response function deconvolved from our simulation (blue line) compared to the response function estimated from reflectometry measurements described in (Patra et al. submitted). Our simulations are in good agreement with the reflectometry results, dropping below -60 dB at 180 ns. Since the foregrounds are $\approx 10^6$ times larger than the signal, the necessary attenuation of zenith emission is obtained after $\approx 0.1 h\text{Mpc}^{-1}$.

ever, comparison between individual frequency channels in both CST and FEKO indicates numerical precision errors **Show a figure of an attempted beam and frequency artifacts at zenith.**

5. THE EFFECT OF THE HERA DISH CHROMATICITY ON FOREGROUND LEAKAGE AND SENSITIVITY

5.1. Simulating Foreground Visibilities with the Spectral Structure of the HERA Dish.

5.2. How Deep Can we Clean?

The level of foreground subtraction possible depends on the number of time steps and redundant baselines that are averaged before performing the cleaning step.

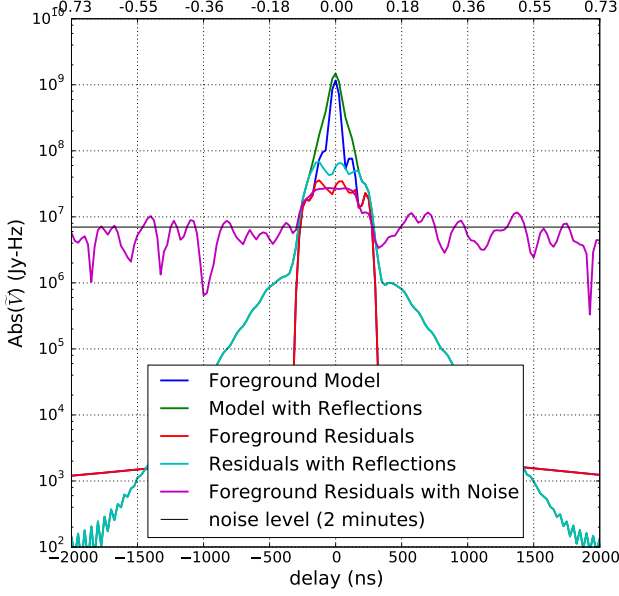


FIG. 6.— The absolute magnitude of a delay transformed 14-meter baseline (blue line) compared to the same visibility (green line) contaminated by reflections at the level observed in the HERA dish design. We see that the extended delay kernel smooths out structure, originating from foregrounds, within the horizon. For HERA, we expect to use the delay-clean to remove foregrounds. However, the depth of cleaning is limited by the noise level on a single baseline (black line). We show the foreground residuals with arising from a clean down to the 5σ noise level after 2 minutes of integration, seeing that cleaning at this cadence achieves \approx two orders of magnitude of foreground reduction. The reflections in the dish lead to extensive winged structures that bleed into the EoR window and are well below the thermal noise level. All data in this plot are obtained from a 100 MHz bandwidth centered at 150 MHz.

The standard deviation on the real and imaginary part of a single delay transformed visibility is given by (?)

$$\Delta V = \frac{\sqrt{2B}k_B T_{sys}}{A_e \sqrt{\tau}} \quad (15)$$

where A_e is the effective area of the dish, B is the bandwidth, T_{sys} is the system temperature, τ is the integration time, and k_B is the Boltzmann constant. The system temperature can be calculated by assuming that $T_{sys} = 100\text{K} + T_{sky}$ where 100K is the temperature of the PAPER receiver and $T_{sky} = 60(\lambda/1\text{ meter})^{2.55}$ is the sky temperature (?). For A_e we use the value of 75 m determined in (Neben et al. submitted). If we assume that each baseline is cleaned independently and that the integration time is $\tau \approx 60\text{s}$, then the noise level at 150 MHz is approximately 9.9 Jy MHz. In order to avoid subtracting noise, we assume that cleaning is performed down to 5σ . In Fig. 6, we see that cleaning to 5σ

5.3. The Implications of Dish Reflections on EoR Science

Since the amplitude of the 21 cm signal is maximal at smaller k values, a loss of large scale signal out to $0.25 h\text{Mpc}^{-1}$ will eliminate some of the power spectrum modes that HERA will have the greatest SNR on, impacting our overall sensitivity. We address the change in SNR and its implications on HERA's ability to place constraints on reionization parameters in this section, using the Fisher Matrix Formalism.

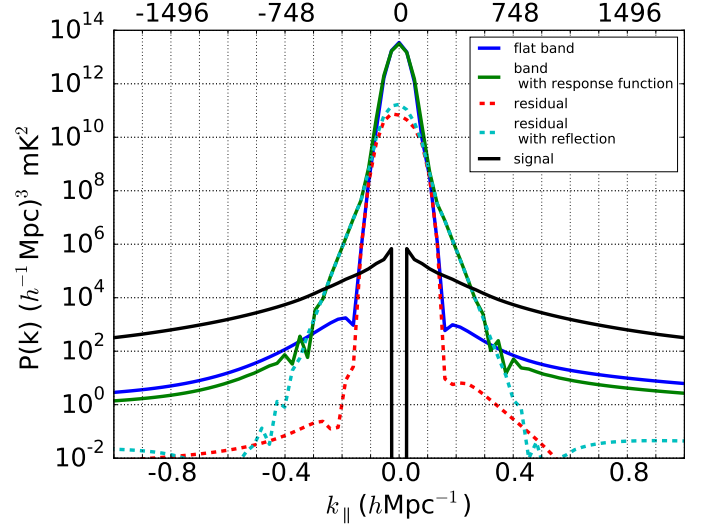


FIG. 7.— The delay transformed power spectra of foregrounds with (blue line) and without (green line) contamination from reflections in the dish. The residuals of these foregrounds, cleaned to 5σ after 2 minutes of integration, are plotted with (red dashed line) and without (cyan dashed line) dish reflections. We compare to the amplitude of the 21 cm power spectrum (solid black line). Foreground contamination, leaked by reflections, extends out to $k_{\parallel} \approx 0.25 h\text{Mpc}^{-1}$. The signals plummet to zero at $k = 0$ is an artifact of the spatial extent of the simulation which does not probe extremely fine scales.

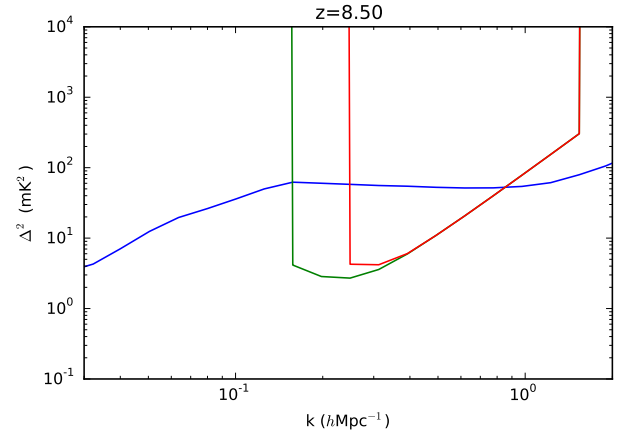


FIG. 8.— Comparison between sensitivities with and without reflections.

constraints on reionization parameters in this section, using the Fisher Matrix Formalism.

6. CONCLUSIONS

REFERENCES

Barry et al. in preparation

Beardsley et al. in preparation

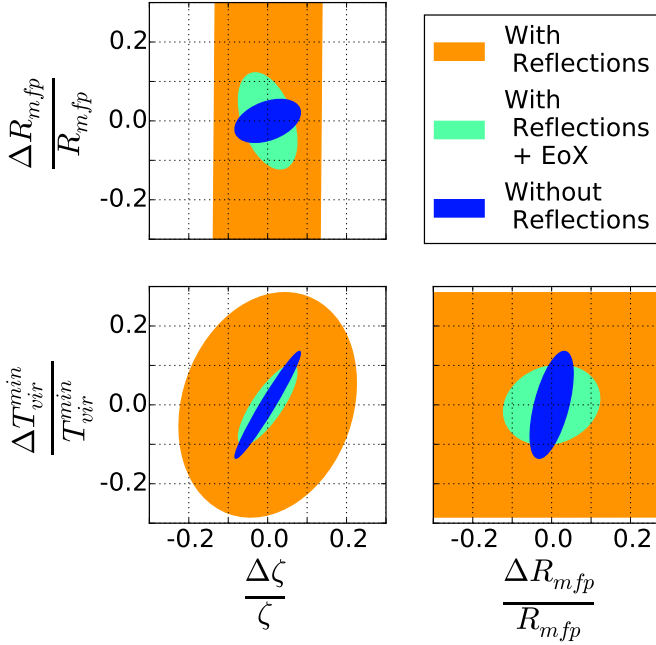


FIG. 9.— 95% confidence intervals with and without reflections. The primary effect of a large minimal delay accessible is that the “knee” which is the primary lever on R_{mfp} becomes inaccessible at low redshift. Since the comoving minimal k corresponding to a minimal delay becomes smaller at higher redshift, EoX measurements do improve constraints on R_{mfp} .

Bowman, J. D., & Rogers, A. E. E. 2010, *Nature*, 468, 796
 Burns, J. O., et al. 2012, *Advances in Space Research*, 49, 433
 Datta, A., Bowman, J. D., & Carilli, C. L. 2010, *ApJ*, 724, 526
 Dillon, J. S., et al. 2015, *Phys. Rev. D*, 91, 123011
 Ewall-Wice, A., et al. submitted 2015, Submitted to *MNRAS*
 Furlanetto, S. R., Oh, S. P., & Briggs, F. H. 2006, *Phys. Rep.*, 433, 181
 Greenhill, L. J., & Bernardi, G. 2012, *ArXiv e-prints*
 Liu, A., Parsons, A. R., & Trott, C. M. 2014a, *Phys. Rev. D*, 90, 023018
 —. 2014b, *Phys. Rev. D*, 90, 023019
 Liu, A., & Tegmark, M. 2011, *Phys. Rev. D*, 83, 103006
 Morales, M. F., & Wyithe, J. S. B. 2010, *ARA&A*, 48, 127
 Neben et al. submitted, *ApJ*
 Paciga, G., et al. 2013, *MNRAS*, 433, 639
 Parsons, A. R., Pober, J. C., Aguirre, J. E., Carilli, C. L., Jacobs, D. C., & Moore, D. F. 2012, *ApJ*, 756, 165
 Parsons, A. R., et al. 2010, *AJ*, 139, 1468
 Patra et al. submitted, *ApJ*
 Pober, J. C., et al. 2014, *ApJ*, 782, 66
 Pritchard, J. R., & Loeb, A. 2012, *Reports on Progress in Physics*, 75, 086901
 Sokolowski, M., et al. 2015, *PASA*, 32, 4
 Thyagarajan, N., et al. 2013, *ApJ*, 776, 6
 —. 2015a, *ApJ*, 807, L28
 —. 2015b, *ApJ*, 804, 14
 Thyagarajan et al. submitted, *ApJ*
 van Haarlem, M. P., et al. 2013, *A&A*, 556, A2
 Vedantham, H., Udaya Shankar, N., & Subrahmanyan, R. 2012, *ApJ*, 745, 176
 Voytek, T. C., Natarajan, A., Jáuregui García, J. M., Peterson, J. B., & López-Cruz, O. 2014, *ApJ*, 782, L9
 Wieringa, M. H. 1992, *Experimental Astronomy*, 2, 203
 Zheng, H., et al. 2014, *MNRAS*, 445, 1084

APPENDIX

THE EFFECT OF REFLECTIONS AND CROSS-TALK ON VISIBILITIES

In this section, we develop formalism to discuss the impact of reflections of electromagnetic waves between antennas and within the signal chain of single antennas on foreground leakage in 21 cm experiments. We start with the time varying electric field from a single source with location $\hat{\mathbf{k}}$ on the sky, arriving at antenna i with delay τ_i and antenna j with delay τ_j with respect to the electric field at the origin which we denote as $s(t, \hat{\mathbf{s}})$. We allow for two different types of reflections: First, we allow reflections within the analogue path of each i^{th} antenna which we denote as $r_i(\tau, \hat{\mathbf{s}})$. We also allow for single reflections between any $i-j$ antenna pair which we denote as $r_{ij}(\tau', \hat{\mathbf{s}})$. Our choice of arbitrary τ' , for now, allows for multi-path propagation between antennas, though we expect it to be dominated by the geometrical delay between the antenna pair. The electric field at antenna i is given by

$$s_i(t, \hat{\mathbf{s}}) = \int d\tau' r_i(\tau', \hat{\mathbf{s}}) s(t + \tau_i - \tau') + \sum_{j \neq i} \int d\tau' s(t + \tau_j - \tau_{ij}) r_{ij}(\tau', \hat{\mathbf{s}}) \quad (\text{A1})$$

In an FX correlator, the electric field is sampled, Fourier transformed, and cross multiplied between antenna pairs to form visibilities. The Fourier transform step leaves us with

$$\tilde{s}_i(f, \hat{\mathbf{s}}) = \tilde{s}(f, \hat{\mathbf{s}}) \left[\int d\tau' r_i(\tau', \hat{\mathbf{s}}) e^{2\pi i(\tau_i - \tau')f} + \sum_{j \neq i} \int d\tau' e^{2\pi i(\tau_j - \tau_{ij})f} r_{ij}(\tau', \hat{\mathbf{s}}) \right] \quad (\text{A2})$$

Multiplying and averaging gives us the visibility for the single source we obtain

$$\begin{aligned} v'_{ij}(f, \hat{\mathbf{s}}) &= \langle \tilde{s}_i(f, \hat{\mathbf{k}}) \tilde{s}_j(f, \hat{\mathbf{s}}) \rangle_t \\ &= d\Omega I(f, \hat{\mathbf{s}}) g_i(f) g_j^*(f) a_i(f, \hat{\mathbf{s}}) a_j^*(f, \hat{\mathbf{s}}) e^{2\pi i \mathbf{u}_{ij} \cdot \hat{\mathbf{s}}} + d\Omega I(f, \hat{\mathbf{s}}) \sum_{\ell \neq j} g_i(f) a_i(f, \hat{\mathbf{s}}) C_{\ell j}^*(f, \hat{\mathbf{s}}) e^{2\pi i \mathbf{u}_{\ell i} \cdot \hat{\mathbf{s}}} \\ &\quad + d\Omega I(f, \hat{\mathbf{s}}) \sum_{k \neq i} g_j^*(f) a_j^*(f) C_{ki}(f, \hat{\mathbf{s}}) e^{2\pi i \mathbf{u}_{kj} \cdot \hat{\mathbf{s}}} + d\Omega I(f, \hat{\mathbf{s}}) \sum_{k \neq i} \sum_{\ell \neq j} C_{ki}(f, \hat{\mathbf{s}}) C_{j\ell}^*(f, \hat{\mathbf{s}}) e^{2\pi i \mathbf{u}_{k\ell} \cdot \hat{\mathbf{s}}}, \end{aligned} \quad (\text{A3})$$

where $g_i(f) a_i(f, \hat{\mathbf{s}}) = \int d\tau r_i(\tau, \hat{\mathbf{s}}) e^{2\pi i f \tau}$ is the effective direction dependent gain of the system which can be factored into a direction dependent and direction independent function where $g_i(f)$ is the gain of the analogue signal chain after

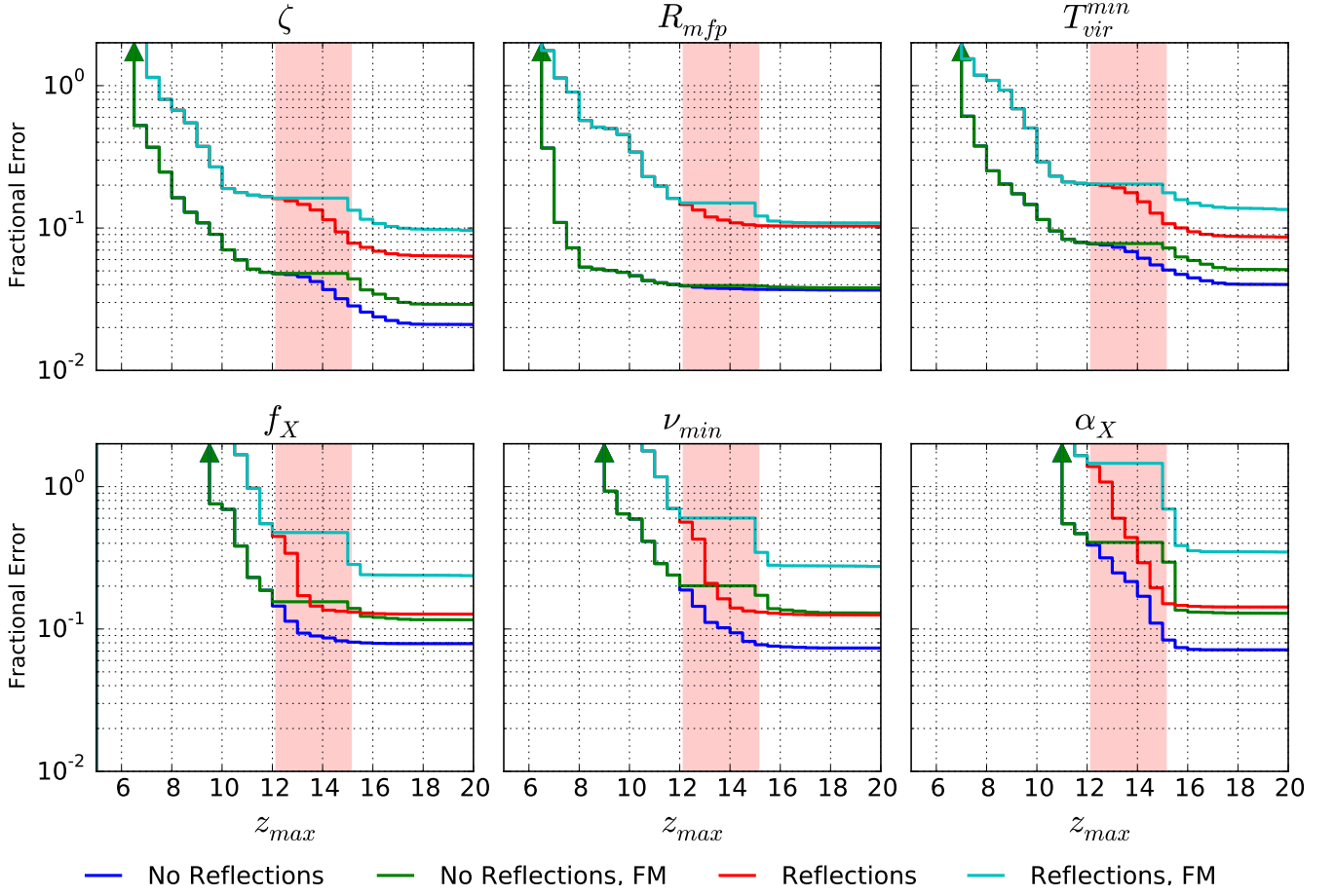


FIG. 10.— Fractional Errors on reionization and heating parameters as a function of maximal observed redshift.

the radiation has been absorbed by the feed and $a_i(f, \hat{s})$ describes the chromatic electric field response of the antenna. The first term in equation A3 is an effective visibility with self-reflections. The two cross terms and the last term involve the mixing of visibilities complementary to the ij baseline and have the potential to introduce significant chromatic features since they potentially insert visibilities on much longer baseline lengths. Assuming propagation along a single path directly between the antennas, we may write $C_{ik}(f, \hat{s})$ as

$$C_{ki}(f, \hat{s}) = a_i(f, \hat{s}_{ki}) \frac{1}{r_{ik}} \left[\frac{d\sigma_k(f, \hat{s}, \hat{s}_{ik})}{d\Omega} \right]^{1/2} e^{2\pi i \tau_{ik} f} \quad (\text{A4})$$

Where r_{ik} is the distance between antennas i and k , $d\sigma_k(f, \hat{s}, \hat{s}_{ij})/d\Omega$ is the cross-section of the antenna to scatter radiation from the \hat{s} direction to the \hat{s}_{ik} direction where \hat{s}_{ik} is the unit vector in the direction between antenna i and antenna k . Integrating over the primary beam, we obtain a full expression on the effect of the foregrounds.

$$V'_{ij} = \int d\Omega v'_{ij}(f, \hat{s}) = g_i(f) g_j(f)^* \int d\Omega A_{ij}(f, \hat{s}) I(f, \hat{s}) e^{2\pi i f \mathbf{u}_{ij} \cdot \hat{s}} + g_i(f) \sum_{\ell \neq j} \int d\Omega A_{i\ell j}(f, \hat{s}) I(f, \hat{s}) e^{2\pi i \mathbf{u}_{\ell i} \cdot \hat{s}} \\ + g_j^*(f) \sum_{k \neq i} \int d\Omega A_{jki}^*(f, \hat{s}) I(\hat{s}, f) e^{2\pi i \mathbf{u}_{kj} \cdot \hat{s}} + \sum_{k \neq i} \sum_{\ell \neq j} \int d\Omega A_{k\ell j}(f, \hat{s}) I(f, \hat{s}) e^{2\pi i \mathbf{u}_{k\ell} \cdot \hat{s}} \quad (\text{A5})$$

which is essentially an admixture of many baselines with different effective primary beams. We denote the effective primary beam of the i, j antenna pair as $A_{ij}(f, \hat{s}) = a_i(f, \hat{s}) a_j^*(f, \hat{s})$, the effective beam from a single reflection correlated with a direct measurement as $A_{i\ell j} = a_i(f, \hat{s}) C_{\ell j}^*(f, \hat{s})$ and the correlation between entirely reflected terms as experiencing an effective primary beam of $A_{k\ell j} = C_{ki}(f, \hat{s}) C_{j\ell}^*(f, \hat{s})$. In this paper, we focus on the reflection terms within a single antenna element. Hence, we ignore all but the first term for now. Any reflection terms occurring downstream of the conversion by the feed from electromagnetic radiation to voltage are lumped into $g_i(f)$ and reflections occurring within the antenna element enter into $a_i(f, \hat{s})$. While reflections within the analogue system are a potential source of contamination, HERA's post-feed analogue signal path is designed to keep all reflections under 35 m, within the wedge.

The focus of this paper and its companions is the reflection properties of the primary antenna element, so we will

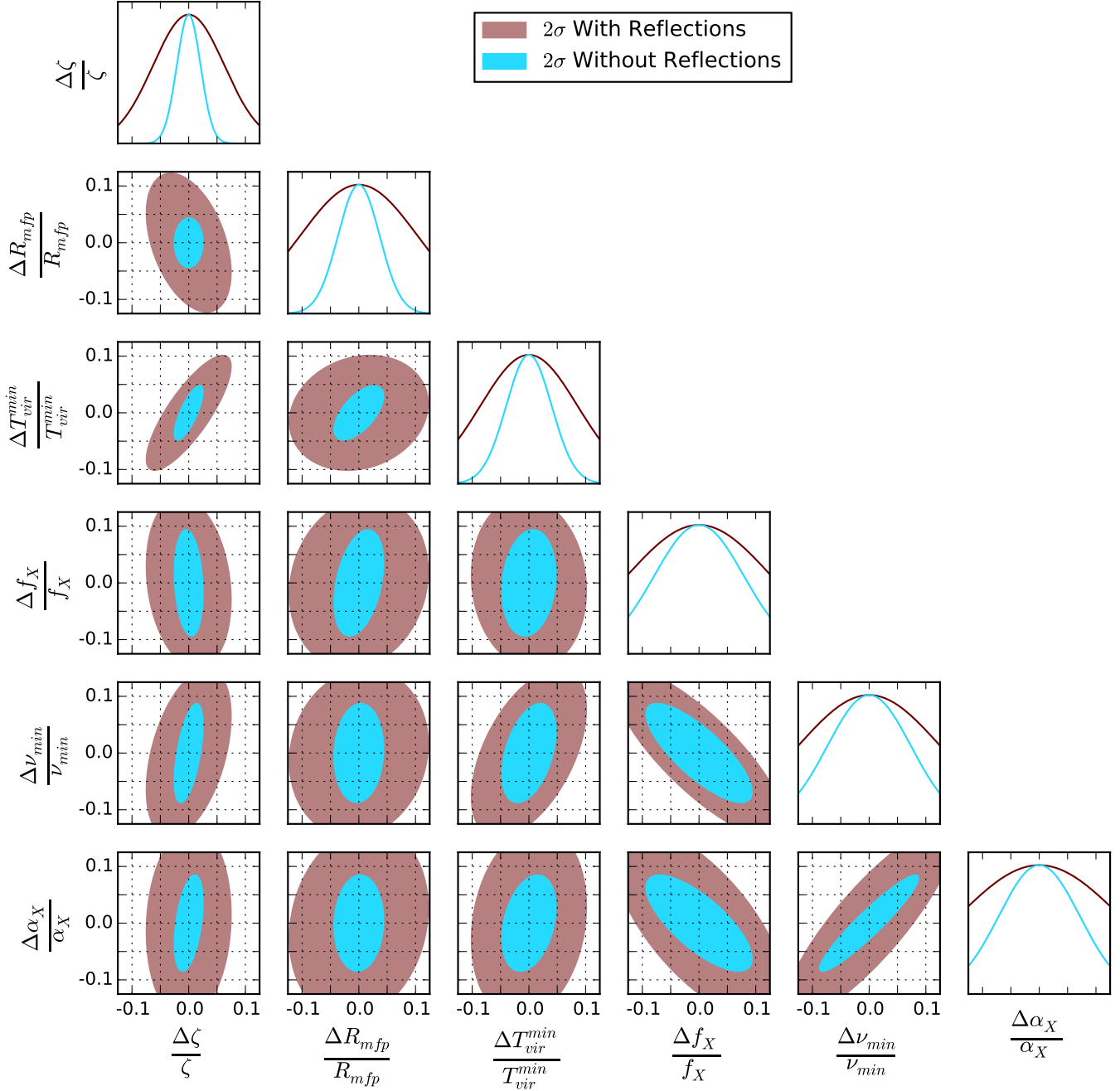


FIG. 11.— 95% confidence regions with and without reflections assuming that observations are taken over the redshifts between 5 and 25 are observed.

focus the rest of our discussion here on $a_i(f, \hat{\mathbf{s}})$. The primary elements of our dish include a feed and backplane suspended over a fourteen meter dish. We assume a set of discrete reflections within the dish, which without loss of generality are assumed to have frequency independent reflection coefficients⁷ hence

$$a_i(f, \hat{\mathbf{s}}) = \sum_n r_n(\hat{\mathbf{s}}) e^{2\pi i \tau_n f} \quad (\text{A6})$$

Assuming all antennas are identical, we have

$$A_{ij}(f, \hat{\mathbf{s}}) = \sum_m \sum_n r_n(\hat{\mathbf{s}}) r_m^*(\hat{\mathbf{s}}) e^{2\pi i (\tau_n - \tau_m) f} = \sum_\alpha A_\alpha(\hat{\mathbf{s}}) e^{2\pi i \tau_\alpha f} \quad (\text{A7})$$

⁷ If we allow each coefficient to be frequency dependent, we can expand each frequency dependent term in a Fourier series of

frequency independent terms

where we have re-indexed m and n under a single greek index α in the second equality. The effect of internal reflections on a visibility is hence

$$V'_{ij} = \sum_{\alpha} \int d\Omega A_{\alpha}(\hat{\mathbf{s}}) e^{2\pi i \tau_{\alpha} f} e^{2\pi i \mathbf{b}_{ij} \cdot \hat{\mathbf{s}} f / c} I(f, \hat{\mathbf{s}}) \quad (\text{A8})$$

Taking the delay transform, one obtains

$$\tilde{V}'_{ij}(\tau) = \sum_{\alpha} \tilde{V}^{\alpha}_{ij}(\tau - \tau_{\alpha}) \quad (\text{A9})$$

where

$$\tilde{V}^{\alpha}_{ij}(\tau) = \int d\tau e^{-2\pi i f \tau} \int d\Omega A_{\alpha}(\hat{\mathbf{s}}) e^{2\pi i \mathbf{b}_{ij} \cdot \hat{\mathbf{s}} f / c} I(f, \hat{\mathbf{s}}) \quad (\text{A10})$$

is the usual delay transform of Parsons et al. (2012). \tilde{V}^{α}_{ij} *alpha*(τ).